Korean J. Chem. Eng., 39(6), 1424-1435 (2022)
DOI: 10.1007/s11814-021-1051-6

pISSN: 0256-1115
eISSN: 1975-7220

CFD prediction of mixing performance for circular and non-circular jet mixing tanks

Apinan Namkanisorn*, Santi Wattananusorn*,†, Winatta Sakdasri, and Eakarach Bumrungthaichaichan***

*Department of Chemical Engineering, School of Engineering, King Mongkut's Institute of Technology Ladkrabang, Bangkok 10520, Thailand
**Program in Food Process Engineering, School of Food Industry, King Mongkut's Institute of Technology Ladkrabang, Bangkok 10520, Thailand

(*Received 13 September 2021 • Revised 30 November 2021 • Accepted 22 December 2021*)

Abstract−Our previous CFD predictions of the circular, elliptic, and square jet mixing tanks were re-analyzed to investigate the highest performance jet mixing tank design and the appropriate mixing performance criterion. So, the mixing performance indicated by overall mixing time and maximum mixing time criteria of these jet mixing tanks was compared. These CFD predictions were carefully developed by using our previous reliable jet mixing tank CFD model. For model validation, reasonable agreement between the predicted mixing times and measurements was observed. The results revealed that circular and non-circular jet flow phenomena were significantly different in the near field jet regions. Further, the elliptic jet mixing tank provided the highest mixing performance because of its highest entrainment and turbulence kinetic energy near the jet boundary. Finally, it can be concluded that the maximum mixing time criterion is a suitable mixing performance indicator.

Keywords: Entrainment, Jet, Mixing Time, Nozzle, RANS

INTRODUCTION

The jet mixing tank is one of the efficient mixing devices in chemical industries because of its simple design, absence of moving parts, inexpensive operating cost, and ease of installation and maintenance. The mixing device was first introduced by Fossett and Prosser [1]. The mixing performance of different components inside the tank is enhanced by high velocity liquid jet produced by the pump. This liquid jet provides liquid recirculation and entrainment inside the mixing vessel.

Over the past half-century, the mixing time correlations for various jet mixing tank designs were obtained experimentally. However, until today, there was no universal jet mixing time correlation. This means that these mixing time correlations are case-specific [2]. Furthermore, the liquid flow and mixing phenomena inside these jet mixing tanks were not available [3]. Consequently, in order to investigate the phenomena inside the jet mixing tanks, computational fluid dynamics (CFD) is adopted by many researchers.

One of the earliest jet mixing tank CFD studies was reported by Brooker [4], who confirmed that the CFD model could predict an acceptable jet mixing time. Patwardhan [5] successfully employed the standard k-epsilon (SKE) turbulence model with modified model constants to predict the concentration profiles of the inclined side entry jet mixing tanks. Furthermore, reasonable agreement on the overall mixing times between CFD simulations and experiments was observed. Note that the predicted overall mixing times were computed by the arithmetic average of the mixing times of four different probe locations. Then, the effects of jet arrangement [6,7], tank shape [8], liquid height [9], jet flow rate [10], jet velocity profile [11], fluid types [12], and others on jet mixing performance were numerically studied.

For jet mixing tank CFD modeling, the SKE model was suggested to predict the jet mixing tanks [5,6,13]. However, these reports contradict the suggestion of Phapatarinan et al. [14] that the realizable k-epsilon (RKE) turbulence model is appropriate to predict the jet mixing times for a wide range of jet inlet velocities. Although the RKE successfully predicted the overall jet mixing times, the discrepancy in concentration profile prediction was still observed. Bumrungthaichaichan et al. [15] later demonstrated that the improper inlet turbulence conditions and flat top liquid surface assumption were the main causes of the discrepancy in concentration profile prediction. Moreover, Bumrungthaichaichan and Wattananusorn [3] proposed the reliable model for circular jet mixing tank CFD simulation. In 2021, Kumar and Vaze [16] attempted to use SKE together with the turbulence boundary condition settings suggested by Bumrungthaichaichan et al. [15] to study the circular jet mixing tank. Their predicted results confirmed that the SKE was not a suitable turbulence model for concentration profile and mixing time predictions.

Generally, for free jets, the mixing performance of non-circular jets (or three-dimensional jets) is better than the circular jets [17]. Furthermore, for both near- and far-field regions, the entrainment of the former jets is greater than that of circular jets [18-20]. Although non-circular jets are more effective than round jets, most of the previous experiments and CFD simulations of jet mixing tanks focus only on the circular jets. That is, only a few non-circular jet mixing tank studies were available. Bumrungthaichaichan [21] recently carried out a non-circular jet mixing tank study, in

†To whom correspondence should be addressed.
E-mail: santi_wattananusorn@hotmail.com, cfdgroup_santi@hotmail.com

which he investigated the mixing performance of circular, elliptic, and square jet mixing tanks. And the results revealed that the circular jet mixing tank provided the shortest overall mixing time, followed by elliptic and square jet mixing tanks, respectively. From these predicted overall mixing times, the bias discussion was reported to support reasons why the commercial nozzle designs inside jet mixing tanks are developed by considering the circular cross-sectional shape.

Overall mixing time is less likely to be a good indicator of performance for some jet mixing tank applications, such as blending the inhibitor to prevent runaway reactions [22,23], emergency cooling systems [24], and so on. Because of the overestimated performance of the jet mixing tank, an unanticipated incident may occur. Furthermore, the overall mixing time is not an appropriate indicator to select the ideal jet mixing tank from a variety of designs. Therefore, to obtain a suitable jet mixing tank design, the maximum mixing time should be adopted instead of the overall mixing time. So, in the present paper, our previous RKE-based CFD predictions of circular jet mixing tank (CJMT), elliptic jet mixing tank (EJMT), and square jet mixing tank (SJMT) were re-analyzed to investigate the highest mixing performance of these jet mixing tank designs. Note that only slight mixing performance improvement is essential for some safety applications, such as inhibitor blending, emergency cooling systems, etc. The jet mixing performance indicated by overall mixing time and maximum mixing time criteria was compared to achieve an appropriate mixing performance criterion. Furthermore, the mean flow and turbulence fields of these jets inside the mixing tanks were re-considered to describe their mixing behaviors.

DESCRIPTION OF CFD MODELING

1. Configurations of Pump-around Jet Mixing Tanks

In this paper, 0.5 m-diameter (D) open pump-around circular and non-circular jet mixing tanks were considered. The water height (H) inside the cylindrical tanks was 0.5 m. A nozzle was installed at the tank base. The angle between the nozzle and flat bottom (θ) was 45°. The outlet pipe diameter (d_o) was 0.0381 m. The outlet pipe was placed at 0.05 m above the tank base (h_o). Three different cross sectional nozzle shapes were studied, including circle, ellipse, and square. The circular equivalent diameter (D_e) based jet Reynolds numbers ($Re_j=\rho D_e U_j/\mu$) of these nozzles were controlled to be identical, having values of about 35,000. As reported by Gutmark and Grinstein [17], the circular-equivalent diameter can be defined as the diameter of a circular jet having an identical non-circular jet discharge area. A schematic of the pump-around jet mixing tank and the necessary coordinate systems is shown in Fig. 1. Further, the details of these jet mixing tanks are summarized in Table 1.

2. Computational Domains and Grid Generations

Three-dimensional pump-around jet mixing tank domains and their grid generations were created with the GAMBIT 2.4.6 program. To obtain the predicted results with higher accuracy, the fine grids should be generated inside the jet near-field and near-wall regions where the viscous effect is predominant. Further, the hexahedral grids that are aligned with the jet flow direction should be controlled to suppress the numerical diffusion. Therefore, the computational domains were split into several volumes to store the hexahedral grid cells easily [3,15]. The grid generation of the jet mixing tank can be represented in Fig. 2.

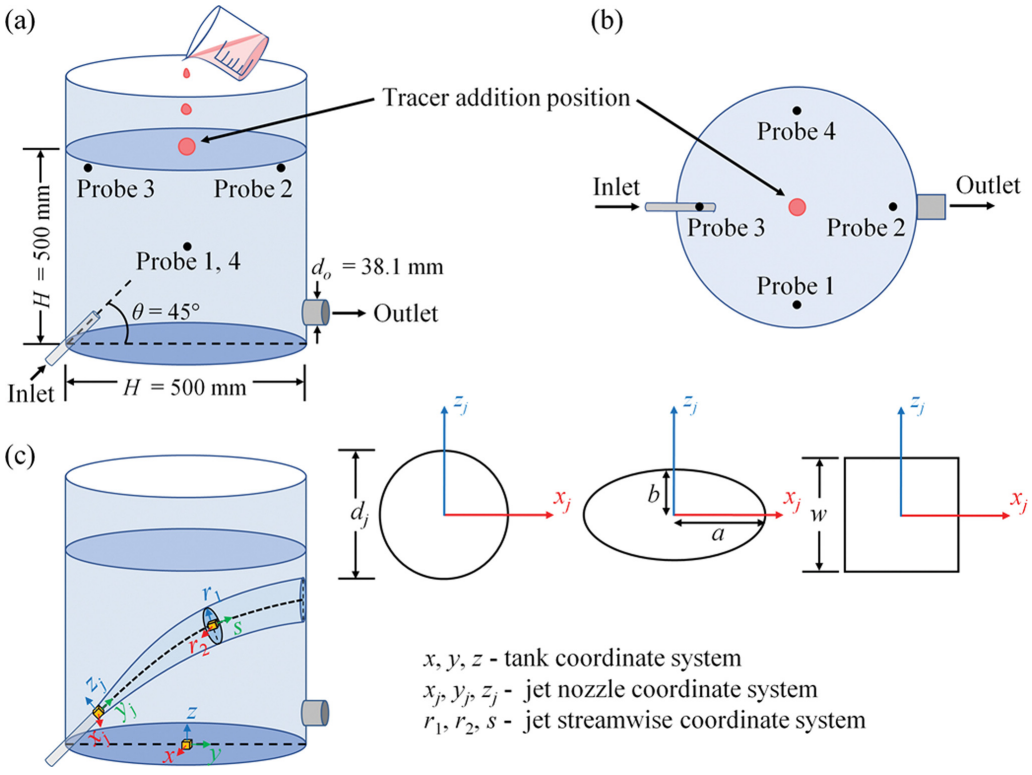

Fig. 1. Schematics of (a) jet mixing tank, (b) jet mixing tank (top view), and (c) coordinate systems and nozzle cross-sectional shapes.

Table 1. Shapes and dimensions of the studied jet mixing tanks

Detail	CJMT	EJMT	SJMT
Tank shape		Cylindrical tank	
Tank diameter (D)		0.5 m	
Liquid height (H)		0.5 m	
Outlet pipe shape		Circular pipe	
Outlet pipe diameter (d_o)		0.0381 m	
Outlet pipe height (h_o)		0.05 m	
Nozzle cross-sectional shape	Circle	Ellipse	Square
Nozzle cross-sectional area (A)		50.27×10^{-6} m^2	
Circular equivalent diameter (D_e)		0.008 m	
Nozzle dimension[a]	$d_j=8\times10^{-3}$ m	$a=5.66\times10^{-3}$ m $b=2.83\times10^{-3}$ m	$w=7.09\times10^{-3}$ m
Nozzle angle (θ)		45°	

[a]d_j, a, b, and w stand for circular nozzle diameter, major radius, minor radius, and width, respectively.

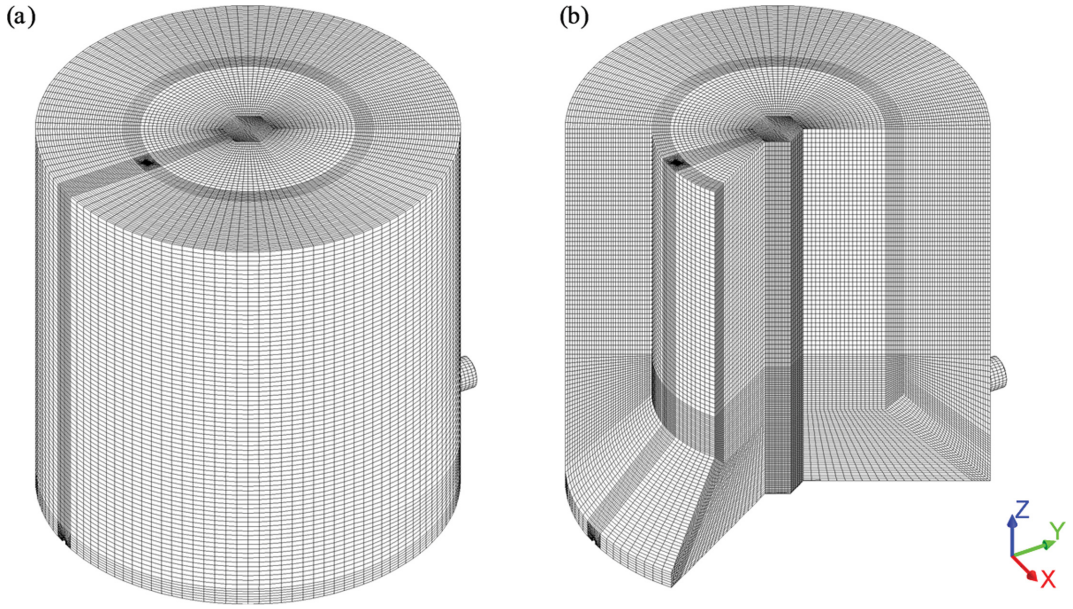

Fig. 2. (a) Surface and (b) Interior grid generations of jet mixing tank.

3. Model Assumptions

In this paper, four assumptions used to obtain the CFD models for pump-around jet mixing tanks were as follows: (i) The liquid jet flow inside the tank was completely developed before the onset of the mixing time investigation. Thus, the CFD simulations were distinguished into two parts, including steady state simulation of the mean flow pattern and time dependent simulation of the concentration distribution. (ii) The properties of liquid water and tracer were identical due to the dilute concentration of the tracer. (iii) The flat top liquid surface was assumed to reduce the computational resources. (iv) The turbulence was predicted by the turbulence model because the mean flow properties are only required to describe the flow phenomena in most engineering applications.

4. Governing Equations

The steady state Reynolds-averaged Navier-Stokes equations (RANS) with RKE turbulence model were employed to achieve the mean flow properties and turbulence inside the jet mixing tanks. The standard model constants of RKE, including $C_1=\max[0.43, \eta/(\eta+5)]$, $C_2=1.9$, $C_{1\varepsilon}=1.44$, $\sigma_k=1$, $\sigma_\varepsilon=1.2$, were specified in transport equations of turbulence kinetic energy (TKE or k) and turbulence kinetic energy dissipation rate (TDR or ε). The unsteady state species transport equations without chemical reaction were adopted to represent the tracer concentration distributions inside these jet mixing tanks. Note that the full descriptions of these governing equations were reported in our previous works (cf. Bumrungthaichaichan and Wattananusorn [3] and Bumrungthaichaichan et al. [15] for more details about the selected governing equations of jet mixing tank simulation).

5. Material Properties and Boundary Conditions

For fluid properties, the density, viscosity, and mass diffusivity of water and tracer were 998.2 kg·m^{-3}, 1.003×10^{-3} kg·m^{-1}·s^{-1}, and 2.3×10^{-9} m^2·s^{-1} [25], respectively. As mentioned, the present CFD

predictions included steady state and transient simulations. For steady state simulation, the boundary condition types for inlet, outlet, wall, and top surface boundaries were velocity-inlet, pressure-outlet, wall with no-slip boundary condition, and symmetry, respectively. At the inlet, the uniform jet discharge velocity (U_j) of 4.4 $m \cdot s^{-1}$ was specified for circular and non-circular jet mixing tank CFD simulations. In addition, for model validation, the circular jet discharge velocities of 6.6, 8.8, and 11 $m \cdot s^{-1}$ were also simulated. The inlet values of k and ε were estimated by $(3/2)(U_jI)^2$, where I is turbulence intensity, and $0.08k^{3/2}/(0.07D_e)$, respectively [15]. For circular jet, the turbulence intensity was 10%. Moreover, the turbulence intensities of 15% [18] and 12% [26] were used to compute the values of k for EJMT and SJMT, respectively. The zero gauge pressure was imposed at the domain outlet and the operating pressure was 101,325 Pa. The standard wall functions [27] were applied to all wall sections.

For transient simulation, the velocity-inlet and pressure-outlet boundary condition types were changed into recirculation-inlet and recirculation-outlet to re-circulate the tracer from tank outlet pipe to inlet jet nozzle as suggested by Bumrungthaichaichan et al. [15]. These extra boundary condition types were enabled by, respectively, typing (rpsetvar 'icepak? #t) and (models-changed) in text user interface [28]. Further, other boundary condition setups were similar to those specified in the steady state simulation.

6. Numerical Setups

The double precision pressure-based solver was selected to omit the round-off error. The pressure-velocity coupling algorithm was SIMPLE. The numerical schemes of gradient and pressure were least squares cell-based and standard, respectively. The second-order upwind spatial discretization scheme was applied for all quantities. The convergence of the steady state simulation was considered when the area-weighted average of velocity magnitude at plane x=0 was constant. For unsteady state simulation, the tracer distribution was resolved on the frozen flow field by using a first-order implicit transient formulation. The time step size was 0.0025 s, which was smaller than time step size computed by the appropriate length and velocity scale approach [2] (Time step size=Length scale/(No. of iteration per time step×Velocity scale)=(0.65 m)/(40×4.4 $m \cdot s^{-1}$)=0.0037 s). This time step size comparison warrants that the selected time step size can be used to simulate the mixing time properly. The tracer scaled residual of 10^{-5} was adopted as a convergence criterion. Note that the lower tracer scaled residual did not improve the accuracy of concentration profile prediction [21].

7. Mixing Time Simulation

According to the experimental study by Patwardhan [5], the dilute NaCl solution was rapidly poured into the tank at the top water surface. Four conductivity probes were used to measure the conductivity at four different positions. The jet mixing criterion was the 95% mixing time, which can be defined as the time required for the concentration (c) to reach 0.95 times fully mixed concentration (C) ($t_{95\%}$=time for $|(c-C)/C| \leq 0.05$).

For unsteady state mixing time simulation, the spherical volume of NaCl tracer was initially specified at 0.03 m below the center of top water surface in order to realize the tracer solution falling downward during the tracer addition. The mass fraction of this tracer was 1. Later, the tracer concentration distribution was iteratively resolved by species transport equations. During this transient calculation, the tracer concentrations at four different positions were collected. The details of four sampling positions (probes) are given in Table 2.

Table 2. Coordinates of concentration sampling positions (probes)

Probe	Tank coordinate system [mm]		
	x	y	z
1	237.5	0	250
2	0	237.5	450
3	0	−237.5	450
4	−237.5	0	250

8. Grid Independent Solutions

In this paper, the effect of grid size on the simulated results was investigated by using the gradient adaption technique (cf. Bumrungthaichaichan et al. [15] for more information about the grid adaption technique). The normalized concentration profiles of CJMT predicted by four different grid resolutions, including 1,087,312 cells (original grids generated by GAMBIT (Coarse)), 1,184,437 cells (1st grid adaptation (Medium)), 1,486,046 cells (2nd grid adaptation (Fine)), and 1,739,978 cells (3rd grid adaptation (Finest)), were compared to obtain grid-independent solutions as depicted in Fig. 3. Note that the normalized concentration was defined as a ratio of the tracer concentration to the fully mixed concentration (c/C). Moreover, the grid convergence index (GCI) was employed to approximate the numerical uncertainties [29] in the form of error bars on the normalized concentration profiles in Fig. 3. Celik et al. [29] used GCI and the average value of the local apparent order of discretization method (p) to obtain the error bars on the spatial profile. For this CFD study, the average apparent order of discretization method (p_{avg}) was also employed to investigate the error bars on the normalized concentration profiles (temporal profiles).

Fig. 3(a) reveals that the normalized concentration profiles of these four grid levels are slightly different. However, for fine and finest grid resolutions, the normalized concentration profiles at two different probe locations are quite similar, especially for probe 2. In Fig. 3(b), the discretization error bars of the normalized concentration profiles at probe 1 and probe 2 were evaluated by using GCI and p_{avg} values of 34.22 and 28.22, respectively. The maximum uncertainty in normalized concentration for probe 1 and probe 2 was $\pm 1.91 \times 10^{-2}$ and $\pm 4.83 \times 10^{-3}$, respectively. Further, the results show that the present CFD model qualitatively predicts the normalized concentration profiles. The agreement between the predicted normalized concentration profile and the experimental data of probe 1 is better than that observed by probe 2. The causes of the discrepancy in normalized concentration profiles between the present CFD simulation and experimental data are the improper inlet turbulence conditions and the overprediction in total momentum available for mixing due to the symmetry boundary condition type at the top water surface [15].

According to these results, it can be summarized that the fine grid level sufficiently produces grid-independent solutions. However, the finest grid resolution was employed for all CFD simulations to avoid any numerical uncertainty. That is, for all simulations,

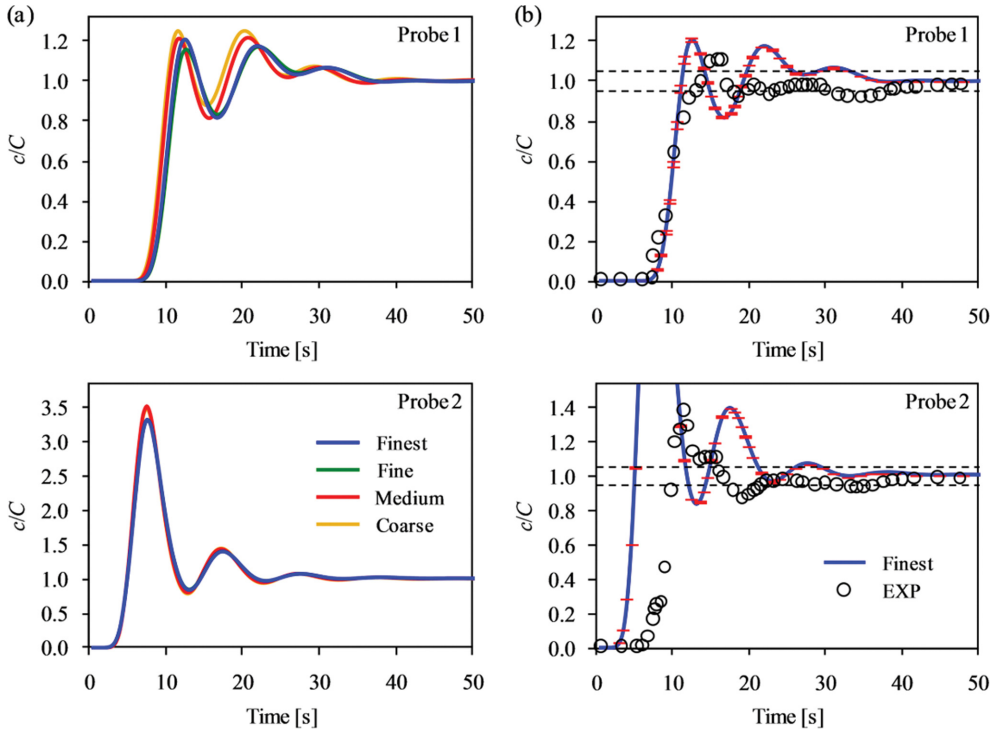

Fig. 3. Normalized concentration profiles for CJMT with jet discharge velocity of 4.4 m·s^{-1} simulated by (a) four grid resolutions and (b) finest grid level with discretization error bars.

the grids were adapted three times to obtain the finest grid level.

9. Model Validation

In the present work, the open 45° inclined side entry pump-around circular jet mixing tanks with jet discharge velocities of 4.4, 6.6, 8.8, and 11 m·s^{-1} were simulated to achieve the CFD model validation. Furthermore, the overall jet mixing times predicted by the current CFD model were compared to Patwardhan's [5] previous numerical and experimental results, as shown in Fig. 4.

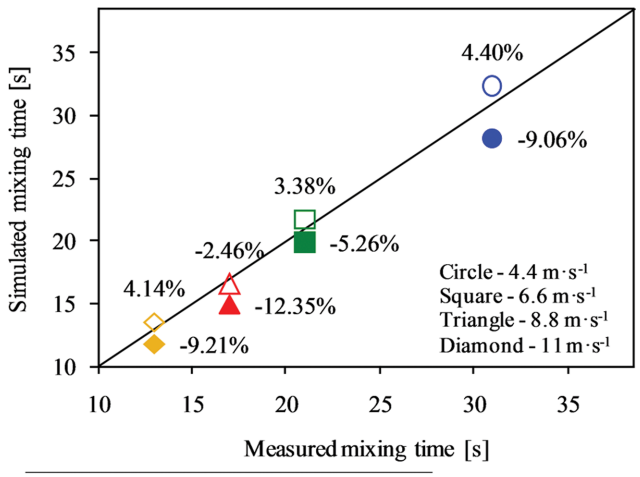

Filled symbols are the present CFD results.
Hollow symbols are the previous CFD results of Patwardhan (2002).

Fig. 4. Comparison of overall mixing times between the current CFD model and Patwardhan's [5] previous work.

From Fig. 4, the results show that the present CFD model underpredicts the overall mixing times for all jet discharge velocities. The maximum percentage error, which was defined as [(predicted mixing time−measured mixing time)/measured mixing time]×100, of the current underpredicted overall mixing times is 12.35%. The agreement between the present predicted overall mixing times and previous experimental results [5] is not as good compared to those predicted by previous CFD work [5]. However, according to the flat top water surface assumption of the present and previous CFD models, the predicted overall mixing times should be lower than those observed experimentally because of the overpredicted total momentum available for mixing [15]. This means that the present CFD model is more reliable for predicting the overall mixing time than the previous CFD model [5]. Finally, from these results, it can be summarized that the present CFD model is acceptably employed to investigate the mixing performance inside the open inclined side entry pump-around jet mixing tank.

RESULTS AND DISCUSSION

1. Bulk Flows Inside Jet Mixing Tanks

The bulk flows of CJMT, EJMT, and SJMT are demonstrated by the mean streamwise velocity (U) contours at planes x_j=0 and z_j=0 as depicted in Fig. 5. From Fig. 5, the bulk transports of these jet mixing tanks are quite similar. The gradual expansions of these jets (jet spreading) are investigated in their lateral directions. In the initial jet regions, the jets axially flow along their centerlines. After the short downstream distances, these jets downward deviate from their centerlines. At the remote areas, the jets impinge on the oppo-

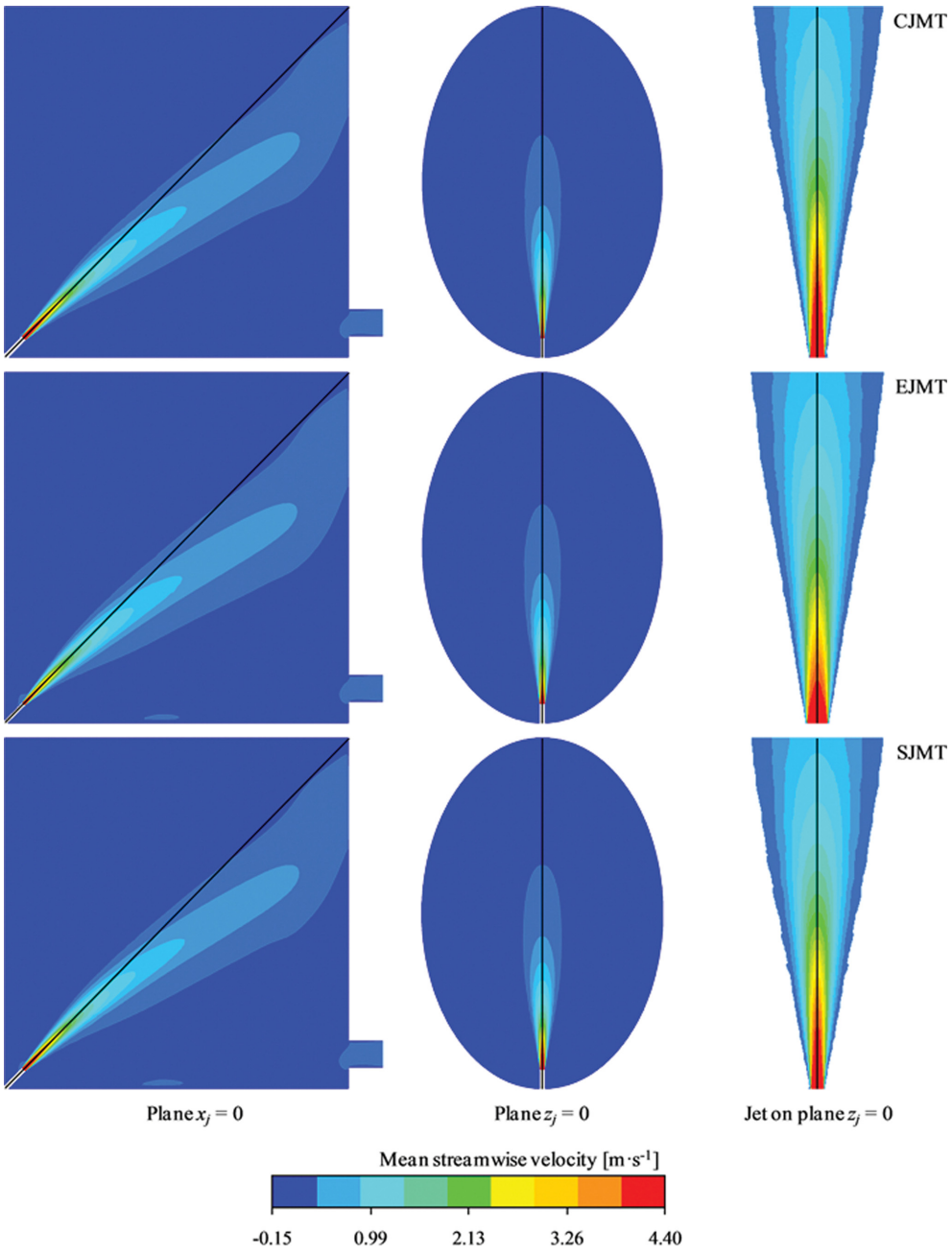

Fig. 5. Mean streamwise velocity contours of different jet mixing tanks.

site walls and create jet rollovers. After the jet rollovers, the water slowly flows along the walls and water surfaces. Then, the water jets entrain the surrounding liquid from remote zones toward the jets. Finally, the jets and their entrained liquids are mixed inside the jets.

2. Jet Flow Phenomena Inside the Mixing Tanks

The spreading of circular, elliptic, and square jets inside the mixing tanks is represented by line contours of the normalized mean streamwise velocity as illustrated in Fig. 6. The normalized mean streamwise velocity was defined as a ratio of mean streamwise velocity to the centerline mean streamwise velocity (U/U_c). Fig. 6 reveals that these jets gradually spread in their jet lateral directions and preserve their initial cross-sectional shapes (nozzle shapes) for $s/D_e \leq 5$. In this region, the spreading rate (S) of an elliptic jet (0.035) is greater than that of a square jet (0.034) and a circular jet (0.018). These spreading rates were evaluated by dr_{eq}/ds, where r_{eq} is an equivalent jet half-width, which can be defined as $r_{eq}=(r_{0.5,\,major} \times r_{0.5,\,minor})^{1/2}$ [30]. Moreover, these line contours qualitatively represent the lateral gradients of mean streamwise velocity of non-circular jets, which are variant in the jet's azimuthal direction. Beyond $s/D_e=5$, the different spreading rates along non-circular jet boundaries due to the non-uniform shear stresses cause the cross-sectional shapes of these jets to trend to approach the cross-sectional shape of the circular jet. The axis-switching phenomenon is not observed during

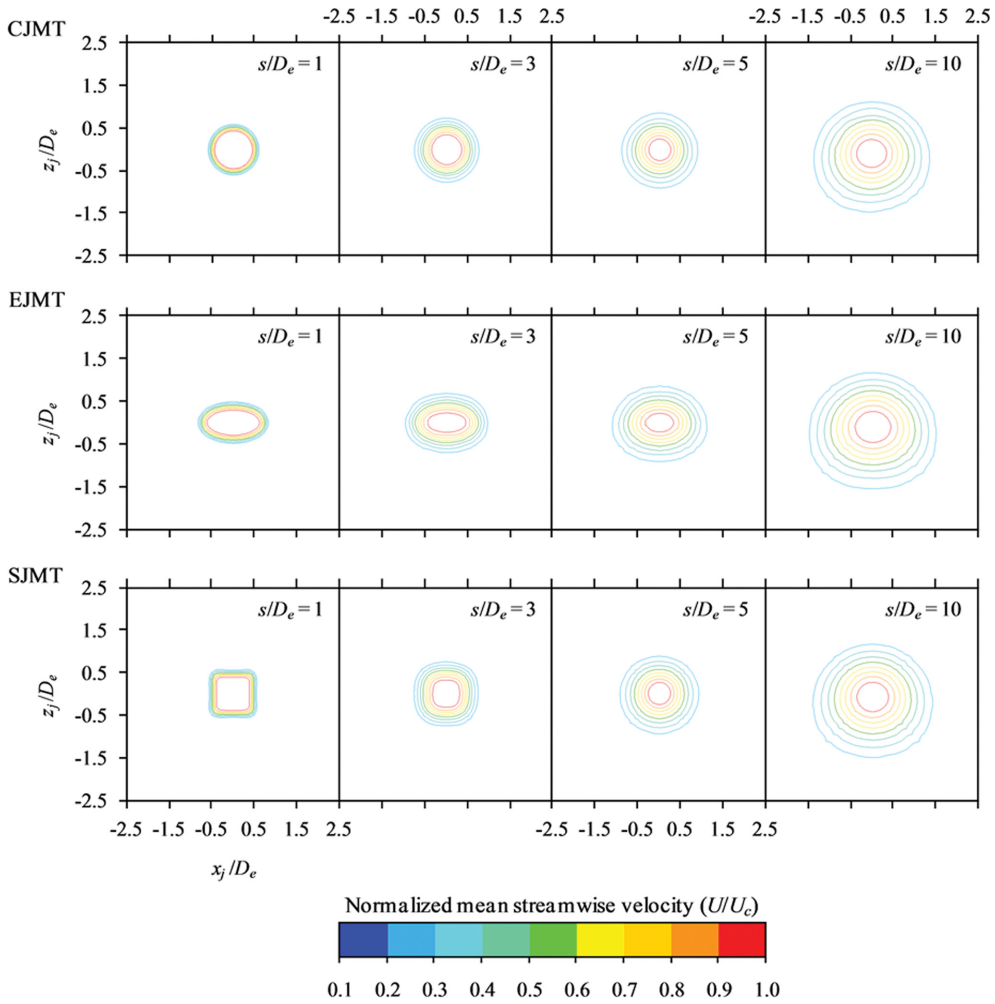

Fig. 6. Line contours of normalized mean streamwise velocity for different jets in the mixing tanks.

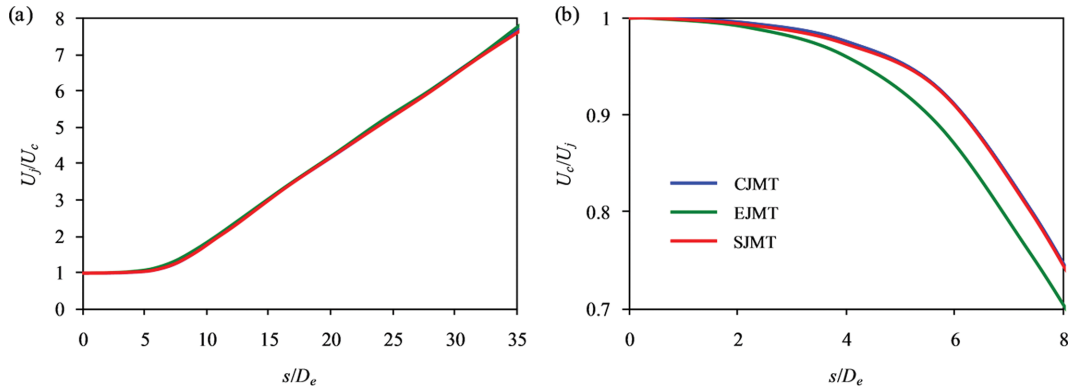

Fig. 7. (a) Inverse mean centerline streamwise velocity decay (b) Decay of mean centerline streamwise velocity at jet near-field region.

non-circular jet development, which corresponds to previous experimental works by Grinstein et al. [19] and Schadow et al. [31].

In general, the wider spread of free jets results in a faster decay of mean centerline streamwise velocity and a greater entrainment rate. For the jets inside mixing tanks, Fig. 7 shows that the tendencies of the predicted mean centerline velocity decays for these jets inside the mixing tanks are similar to the previous free jet experiments of Mi et al. [32]. That is, the elliptic jet provides the fastest decay of the mean centerline streamwise velocity, followed by the square and circular jets. For $s/D_e>15$, the mean centerline velocity decays inside these jet mixing tanks are insignificantly different. Table 3 shows that an elliptic jet can attain the highest entrainment ratios at different positions (18-42% higher than circular jet). Furthermore, the entrainment ratios of a square jet are about 6-14%

Table 3. Entrainment ratios of different jets in the mixing tanks

s/D_e	Entrainment ratio[a]		
	CJMT	EJMT	SJMT
1	0.17	0.23	0.19
3	0.49	0.66	0.53
5	0.88	1.14	0.94
10	2.25	2.67	2.39

[a]Entrainment ratio is defined as $(Q-Q_0)/Q_0$ [18], where Q is a local mass flow rate and Q_0 is a nozzle exit mass flow rate (0.22 $kg \cdot s^{-1}$).

better than those obtained by a circular jet.

In addition, the greater entrainment typically induces higher turbulence kinetic energy near the jet edge. So, the radial profiles of the normalized turbulence kinetic energy, which was a ratio of turbulence kinetic energy to the square of jet discharge velocity (k/U_j^2), for circular, elliptic, and square jets at different positions were compared as represented in Fig. 8. In Fig. 8, the saddle-backed and bell-like profiles of these jets are observed at $s/D_e \leq 5$ and $s/D_e=10$, respectively. Furthermore, due to the higher spreading rates of non-circular jets, the centerline turbulence kinetic energy decays faster for non-circular jets than for circular jet. However, at the regions near jet boundaries, the elliptic jet has the largest turbulence kinetic energy, followed by square and circular jets. This is because non-circular jets extract energy from the mean flow, resulting in a reduction of vorticity strength, as shown in Fig. 9. In Fig. 9, the circular jet provides a greater strength of vorticity than non-circular jets due to the absence of the mean flow energy extraction required for adjusting the jet cross-sectional shape driven by the non-uniform shear stress distribution along the jet boundary.

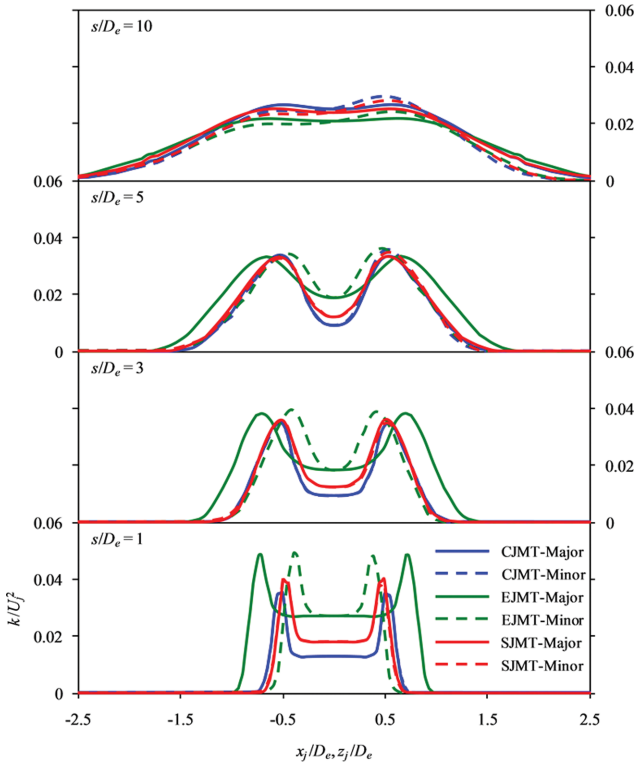

Fig. 8. Radial profiles of normalized turbulence kinetic energy for different jets in the mixing tanks.

3. Jet Mixing Performance

At four distinct probe locations, Fig. 10 depicts the normalized concentration profiles of three different jet mixing tank designs. Except for the profile of CJMT at probe 4, the normalized concentration profiles of these jet mixing tanks are quite similar. For CJMT, the rise of the predicted normalized concentration profile at probe 1 is faster than that obtained by probe 4 because of the higher con-

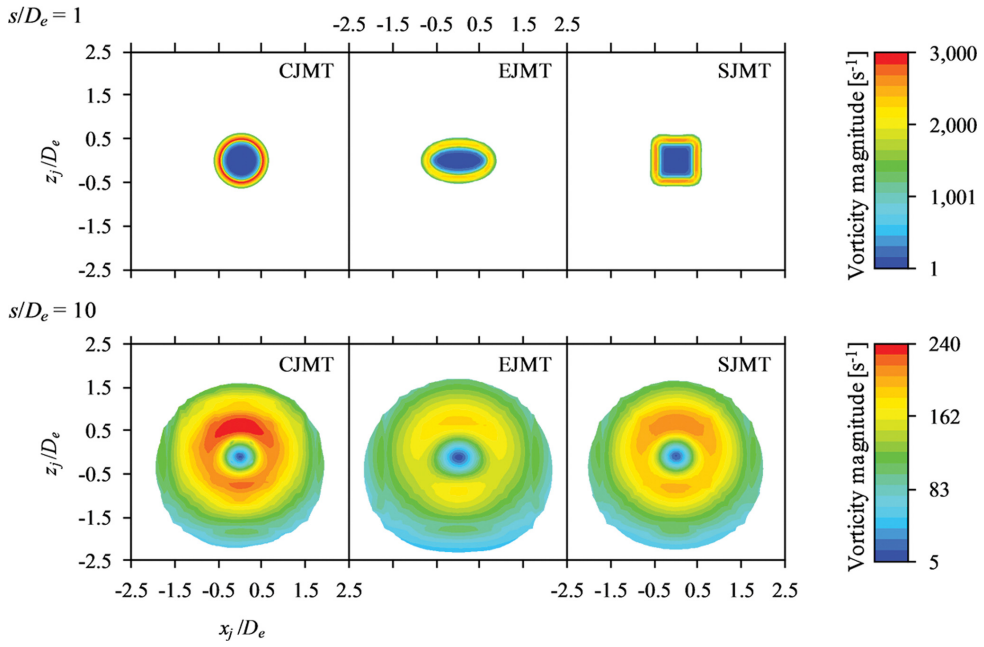

Fig. 9. Contours of vorticity magnitude for different jets in the mixing tanks at $s/D_e=1$ and $s/D_e=10$.

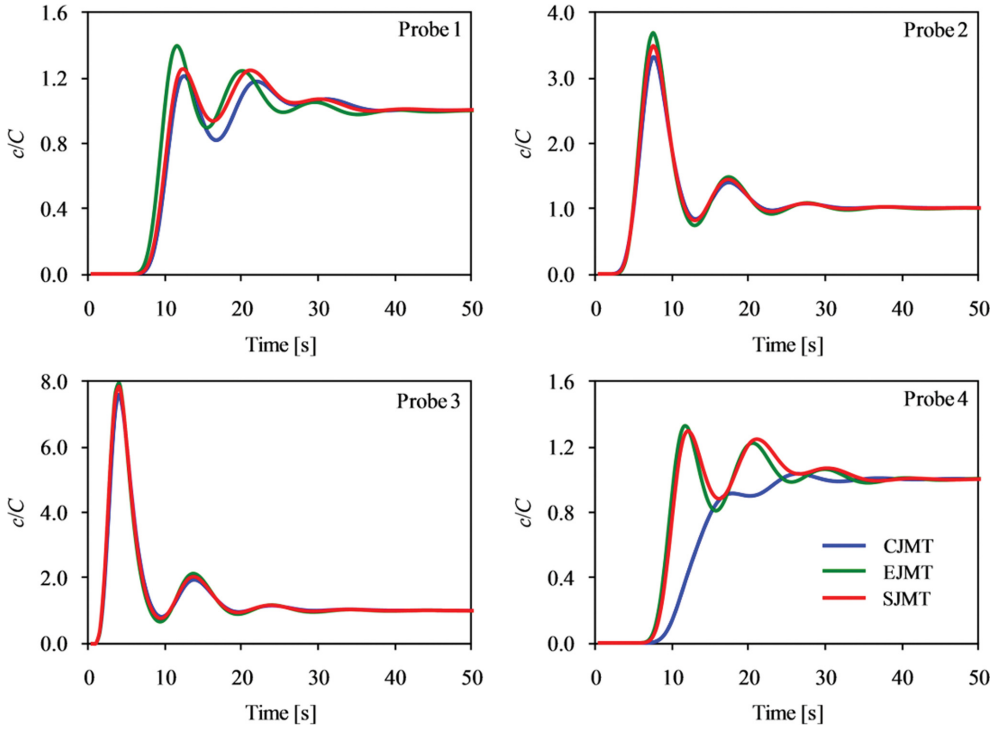

Fig. 10. Normalized concentration profiles for different jet mixing tanks and probe locations.

Table 4. Mixing times of different jet mixing tanks

Design	Mixing time [s]						% Difference[a]
	Probe 1	Probe 2	Probe 3	Probe 4	Overall	Maximum	
CJMT	33.18	29.54	27.30	22.74	28.19	33.18	17.69
EJMT	30.36	29.48	26.70	31.22	29.44	31.22	6.04
SJMT	32.42	29.39	26.93	32.34	30.27	32.42	7.11

[a]Percentage difference is [(Maximum mixing time−Overall mixing time)/Overall mixing time]×100.

vective transport due to the reason that the circular jet is slightly deviated from its centerline towards probe 1, as depicted in Fig. 5 (Jet on plane z_j=0). The rise and first peak values of the normalized concentration profiles for EJMT are, respectively, faster and greater than those predicted by other jet mixing tanks as observed at probes 1, 2 and 4. Although the very weak liquid motions flow along the liquid surface after jet rollover, EJMT still provides the highest first peak value at probe 3, followed by SJMT and CJMT, respectively. The faster rise and greater first peak values of the normalized concentration profiles for EJMT are caused by the higher convective transport [15]. The higher convective transport may give the advantage to EJMT for providing the better mixing performance.

In this paper, the jet mixing times were investigated by considering the normalized concentration profiles and 95% mixing time criterion. Table 4 summarizes the predicted mixing times of four probe locations for these jet mixing tanks. In addition, as shown in Table 4, the overall mixing time criterion suggested by Patwardhan [5] and the maximum mixing time criterion indicated by this study were used to indicate the mixing performance of these jet mixing tanks.

From Table 4, the results reveal that the mixing times are dependent on probe locations and jet mixing tank designs. For overall mixing time criterion, CJMT shows the shortest mixing time, followed by EJMT and SJMT, respectively. Whereas, for the maximum mixing time criterion, the mixing performance of non-circular jet mixing tanks is better than that achieved by CJMT. The best mixing performance is achieved by EJMT. The mixing performance of SJMT is superior to that of CJMT. Furthermore, the mixing performance indicated by overall mixing time is 17.69% better than the mixing performance obtained by the maximum mixing time for CJMT.

4. Discussion

The mixing time predictions were performed after the jet flows inside the mixing tanks had been completely simulated, as previously stated. The frozen flow and turbulence fields inside the tested jet mixing tanks were used to resolve the tracer concentration distributions. The frozen field method can reduce computational resources. It can also be used to track solid particles inside cyclone separators [33-35]. Here, it can be stated that the tracer concentra-

Table 5. Jet phenomena and mixing performances of different jet mixing tanks

Phenomenon/Mixing	CJMT	EJMT	SJMT
Lateral gradient of U in the azimuthal direction	Uniform	Non-uniform	Non-uniform
Spreading rate	Slow	Fast	Medium
Entrainment	Low	High	Medium
TKE near jet boundary region	Low	High	Medium
Vorticity magnitude	High	Low	Medium
Overall mixing time (Lower is better)	Low	Medium	High
Maximum mixing time (Lower is better)	High	Low	Medium

tion distributions were dependent on the jet flows inside the mixing tanks. So, the lateral gradients of mean streamwise velocity, spreading rates, entrainments, turbulence kinetic energy, vorticity magnitudes, overall mixing times, and maximum mixing times of CJMT, EJMT, and SJMT are viewed together to investigate the highest mixing performance of the open 45° inclined side entry pump-around jet mixing tank as shown in Table 5.

From Table 5, the overall mixing time and maximum mixing time criteria indicate that CJMT and EJMT provide the highest mixing performance. One question arises in this situation: which jet mixing tank design delivers the best mixing performance? In order to answer this question, the jet flow behavior was considered and analyzed. From the present results, it can be seen that the jet flows of circular and non-circular jets are different, especially for near field regions of the jets. For non-circular jets, the nozzle cross-sectional shapes promote the lateral gradients of mean streamwise velocity to be variant in the jet azimuthal direction. These non-uniform gradients result in the non-uniform shear stresses near the jet boundary regions. Then, the spreading rates of non-circular jets are greater than that of circular jet. Due to the faster spreading rates of the non-circular jets, although the centerline mean streamwise velocity decays of non-circular jets are faster than that obtained by circular jet, the non-circular jets can produce higher entrainments and turbulence kinetic energy near jet boundaries. It is worth noting that the turbulence kinetic energy is an indirect parameter to identify the mixing due to the effects of velocity fluctuations. In addition, the non-circular jets represent lower vorticity magnitudes than circular jet because they extract energy from their mean flow to adjust their cross-sectional shapes during the jet expansions.

Generally, the mixing performance of free jets can be enhanced by increasing the entrainment rate and velocity fluctuation level [17]. The answer to the above question is that the highest performance jet mixing tank design is EJMT because elliptic jet provides the highest entrainment and turbulence kinetic energy near the jet boundary, similar to the free jet information. Due to the broadest spreading of the jet, this elliptic jet behavior can increase the mixing opportunity between the entrained fluid and the jet stream inside the region near the jet boundary and improve the bulk mixing inside the tank. The current result contradicts Bumrungthaichaichan's [21] prior finding that the CJMT had the best performance due to the slowest centerline turbulence kinetic energy decay and the largest vorticity magnitudes. These circular jet phenomena support the mixing between primary and surrounding fluids inside the jet stream and are only efficient when the surrounding fluid penetrates into the jet centerline. However, the bulk mixing inside the jet mixing tank may not be improved by this circular jet flow behavior because of their low spreading rate and entrainment.

In addition, based on the foregoing discussion, it can be stated that, while Patwardhan [5] reported that the overall mixing time was successfully used to identify the performance of jet mixing tanks with different jet discharge velocities, the overall mixing time is an inappropriate indicator for comparing the mixing performance of different jet mixing tank designs. Furthermore, using the overall mixing time to evaluate jet mixing performance is ineffective since it always overestimates jet mixing performance. It may be concluded that the maximum mixing time is a better representation of mixing performance than the overall mixing time.

CONCLUSIONS

This paper re-analyzed our previous RKE-based CFD predictions of CJMT, EJMT, and SJMT because the earlier study employed an unsuitable overall mixing time criterion to investigate the highest mixing performance of the different jet mixing tank designs [21]. To obtain a suitable mixing performance indicator, the mixing performance indicated by overall mixing time and maximum mixing time criteria was compared. The CFD predictions of three different jet mixing tank designs were properly developed by using our reliable CFD model for circular pump-around jet mixing tanks [3,15]. The inlet turbulence boundary conditions for non-circular jet mixing tanks were obtained by previous experimental data of free jets [18,26]. The error bars on the predicted normalized concentration profiles of CJMT were successfully assessed by GCI. The maximum uncertainty in normalized concentration is about 0.02. For CFD model validation, the present predicted overall mixing times of CJMT for different jet discharge velocities are more reliable than those simulated by the previous CFD model [5] and reasonably agree with the earlier measurements [5]. Finally, the following are the conclusions of the current CFD predictions:

(1) The bulk flows inside CJMT, EJMT, and SMT are quite similar. However, in the near-field regions of the jets, the local flow phenomena of circular and non-circular jets are significantly different because of their nozzle cross-sectional shapes.

(2) The tendencies of jet flow phenomena inside the mixing tanks are similar to those observed by free jet flows [17,19,31].

(3) Due to the nozzle cross-sectional shapes, the elliptic and square jets provide higher jet spreading rates inside the tanks than circular jet because of the variations in the lateral gradients of the

mean streamwise velocity in azimuthal direction, which cause non-uniform shear stresses in the jet boundary regions. These non-uniform shear stresses promote the cross-sectional shape adjustments of non-circular jets. Although the rapid lateral expansions of these non-circular jets result in a faster decay of centerline mean streamwise velocity and lower vorticity magnitude than those of circular jet, however, the higher entrainment and higher turbulence kinetic energy near the jet boundary region are achieved. These non-circular jet flows support the mixing performance improvement for the jet mixing tanks. Further, the elliptic jet flow behavior is better than the flow phenomena of the square jet.

(4) The overall mixing time and the maximum mixing time criteria reveal that the CJMT and EJMT are the highest mixing performance designs, respectively. However, the flow behavior of elliptic jet is more advantageous for improving the mixing inside the tank than that obtained by the circular jet. For the maximum mixing time criterion, the mixing performance of the EJMT is about 6% better than the conventional design (CJMT). So, the highest mixing performance design is EJMT.

(5) The overall mixing time criterion always overestimates the mixing performance inside the jet mixing tank. Therefore, the overall mixing time is a risky mixing performance indicator for some crucial applications, e.g., inhibitor blending, emergency cooling systems, etc. According to the above conclusion, the maximum mixing time is an appropriate indicator to identify the mixing performance of the jet mixing tank.

ACKNOWLEDGEMENTS

The ANSYS FLUENT CFD software was supported by College of Advanced Manufacturing Innovation, King Mongkut's Institute of Technology Ladkrabang, Thailand.

STATEMENT

Apinan Namkanisorn: Conceptualization, Methodology, Validation, Writing - Review & Editing, Supervision, Project administration, Santi Wattananusorn: Conceptualization, Validation, Formal analysis, Writing - Review & Editing, Project administration, Winatta Sakdasri: Writing - Original Draft, Visualization, Eakarach Bumrungthaichaichan: Software, Formal analysis, Investigation, Data Curation, Writing - Original Draft.

DECLARATION OF CONFLICT OF INTEREST STATEMENT

The authors declare that they have no known competing financial interests or personal relationships that could have appeared to influence the work reported in this paper.

NOMENCLATURE

Alphabetical Symbols

a : major radius of elliptic nozzle [m]
A : nozzle cross-sectional area [m^2]
b : minor radius of elliptic nozzle [m]
c : concentration (mass fraction)
C : fully mixed concentration (mass fraction)
C_1, C_2 : constants of RKE turbulence model
$C_{1\varepsilon}$: constant for dissipation rate model of RKE turbulence model
d_j : circular nozzle diameter [m]
d_o : outlet pipe diameter [m]
D : tank diameter [m]
D_e : circular equivalent diameter [m]
h_o : height between outlet pipe centerline and tank bottom [m]
H : water height [m]
I : turbulence intensity
k : turbulence kinetic energy (TKE) [$m^2 \cdot s^{-2}$]
p : local apparent order of discretization method
p_{avg} : average apparent order of discretization method
Q : local mass flow rate [$kg \cdot s^{-1}$]
Q_0 : nozzle exit mass flow rate [$kg \cdot s^{-1}$]
r_1, r_2 : radial coordinates of jet
$r_{0.5,\,major}$: jet half-width for major axis [m]
$r_{0.5,\,minor}$: jet half-width for minor axis [m]
r_{eq} : equivalent jet half-width [m]
Re_j : circular equivalent diameter based jet Reynolds number
s : streamwise coordinate of jet or jet streamwise distance [m]
S : spreading rate
$t_{95\%}$: 95% mixing time [s]
U : mean streamwise velocity [$m \cdot s^{-1}$]
U_c : centerline mean streamwise velocity [$m \cdot s^{-1}$]
U_j : jet discharge velocity [$m \cdot s^{-1}$]
w : width of square nozzle [m]
x : x-coordinate of tank
x_j : x-coordinate of nozzle
y : y-coordinate of tank
y_j : y-coordinate of nozzle
z : z-coordinate of tank
z_j : z-coordinate of nozzle

Greek Symbols

ε : turbulence kinetic energy dissipation rate (TDR) [$m^2 \cdot s^{-3}$]
η : RKE turbulence model parameter
θ : angle between nozzle centerline and tank bottom [°]
μ : viscosity of fluid [$kg \cdot m^{-1} \cdot s^{-1}$]
ρ : density of fluid [$kg \cdot m^{-3}$]
σ_k : turbulence Prandtl number for turbulence kinetic energy
σ_ε : turbulence Prandtl number for turbulence dissipation rate

Abbreviations

CFD : computational fluid dynamics
CJMT : circular jet mixing tank
EJMT : elliptic jet mixing tank
GCI : grid convergence index
RANS : Reynolds-averaged Navier-Stokes equations
RKE : realizable k-epsilon turbulence model
SIMPLE : semi-implicit method for pressure-linked equations
SJMT : square jet mixing tank

SKE : standard k-epsilon turbulence model

REFERENCES

1. H. Fossett and L. E. Prosser, *Proc. Inst. Mech. Eng.*, **160**, 224 (1949).
2. E. Bumrungthaichaichan, *Korean J. Chem. Eng.*, **33**(11), 3050 (2016).
3. E. Bumrungthaichaichan and S. Wattananusorn, *J. Chin. Inst. Eng.*, **42**(5), 428 (2019).
4. L. Brooker, *Chem. Eng.*, **30**, 16 (1993).
5. A. W. Patwardhan, *Chem. Eng. Sci.*, **57**(8), 1307 (2002).
6. H. D. Zughbi and I. Ahmad, *Ind. Eng. Chem. Res.*, **44**(4), 1052 (2005).
7. N. Jaiklom, E. Bumrungthaichaichan and S. Wattananusorn, *Ladkrabang Eng. J.*, **30**(4), 37 (2013).
8. T. Raja, P. Kalaichelvi and N. Anantharaman, *J. Sci. Ind. Res.*, **66**(7), 522 (2007).
9. E. Bumrungthaichaichan, N. Jaiklom, A. Namkanisorn and S. Wattananusorn, *Sci. Res. Essays*, **11**(4), 42 (2016).
10. H. D. Zughbi and M. A. Rakib, *Chem. Eng. Comm.*, **189**(8), 1038 (2002).
11. T. Jorakit, N. Phaiboonsilpa, A. Namkanisorn, P. Ponpo, E. Bumrungthaichaichan and S. Wattananusorn, *MATEC Web of Conferences*, **192**, 03019 (2018).
12. K. K. Sendilkumar, P. Kalaichelvi, M. Perumalsamy, A. Arunagiri and T. Raja, in *World Congress on Engineering and Computer Science 2007*, San Francisco, U.S.A. (2007).
13. H. D. Zughbi and M. A. Rakib, *Chem. Eng. Sci.*, **59**(4), 829 (2004).
14. S. Phapatarinan, E. Bumrungthaichaichan and S. Wattananusorn, *MATEC Web of Conferences*, **192**, 03010 (2018).
15. E. Bumrungthaichaichan, A. Namkanisorn and S. Wattananusorn, *J. Chin. Inst. Eng.*, **41**(7), 612 (2018).
16. D. Kumar and M. Vaze, in *2nd National and 1st International conference on Fluid Flow and Thermal Sciences*, India, ICAFFTS-2021-MF-H178 (2021).
17. E. J. Gutmark and F. F. Grinstein, *Annu. Rev. Fluid Mech.*, **31**, 239 (1999).
18. C. M. Ho and E. J. Gutmark, *J. Fluid Mech.*, **179**, 383 (1987).
19. F. F. Grinstein, E. J. Gutmark and T. Parr, *Phys. Fluids*, **7**, 1483 (1995).
20. K. B. M. Q. Zaman, *AIAA Pap.*, 96-0200 (1996).
21. E. Bumrungthaichaichan, *Computational fluid dynamics simulations of pump-around jet mixing tanks*, Doctoral thesis, King Mongkut's Institute of Technology Ladkrabang (2019).
22. D. Mewes and R. Renz, in *7th European Conference on Mixing*, Belgium, 131 (1991).
23. P. D. Hoffman, *AIChE Symp. Ser.*, **286**(88), 77 (1996).
24. R. Schimetzek, A. Steiff and P. M. Weinspach, *IChemE Symp. Ser.*, **136**, 391 (1995).
25. M. Spyrou, *The diffusion coefficient of water: A neutron scattering study using molecular dynamics simulations*, Master thesis, University of Surrey (2009).
26. W. R. Quinn and J. Militzer, *Phys. Fluids*, **31**(5), 1017 (1988).
27. ANSYS Inc., *ANSYS Fluent Theory Guide: Release 15.0*, U.S.A. (2013).
28. S. Dange, *Recirculation Boundary Conditions in ANSYS FLUENT*, [Online] Available: https://www.learncax.com/knowledge-base/blog/by-category/cfd/recirculation-boundary-conditions-i-ansys-fluent (2016).
29. I. B. Celik, U. Ghia, P. J. Roache, C. J. Freitas, H. Coleman and P. E. Raad, *J. Fluids Eng.-Trans. ASME*, **130**(7), 078001-1 (2008).
30. F. Hussain and H. S. Husain, *J. Fluid Mech.*, **208**, 257 (1989).
31. K. C. Schadow, K. J. Wilson and M. J. Lee, *J. Propuls. Power*, **3**(2), 145 (1987).
32. J. Mi, G. J. Nathan and R. E. Luxton, *Exp. Fluids*, **28**(1), 93 (2000).
33. K. Elsayed and C. Lacor, *Comput. Fluids*, **68**, 134 (2012).
34. P. Pechmanee, A. Namkanisorn, S. Wattananusorn and E. Bumrungthaichaichan, *Comput. Aided Chem. Eng.*, **50**, 529 (2021).
35. E. Bumrungthaichaichan, *Powder Technol.*, **396**, 327 (2022).